The Astrophysical Journal, 959:3 (12pp), 2023 December 10 https://doi.org/10.3847/1538-4357/ad04d2


# Massive Black Hole Binaries from the TNG50-3 Simulation. II. Using Dual AGNs to Predict the Rate of Black Hole Mergers

Kunyang Li[1,2], Tamara Bogdanović[1], David R. Ballantyne[1], and Matteo Bonetti[3,4]
[1] School of Physics and Center for Relativistic Astrophysics, 837 State St. NW, Georgia Institute of Technology, Atlanta, GA 30332, USA; likun@iap.fr, tamarab@gatech.edu, david.ballantyne@physics.gatech.edu
[2] Institut d'Astrophysique de Paris, 98bis Bd. Arago, Paris F-75014, France
[3] Dipartimento di Fisica G. Occhialini, Università di Milano-Bicocca, Piazza della Scienza 3, I-20126 Milano, Italy; matteo.bonetti@unimib.it
[4] INFN, Sezione di Milano-Bicocca, Piazza della Scienza 3, I-20126 Milano, Italy
*Received 2022 July 28; revised 2023 September 26; accepted 2023 September 26; published 2023 November 28*

## Abstract

Dual active galaxy nuclei (dAGNs) trace the population of post-merger galaxies and are the precursors to massive black hole (MBH) mergers, an important source of gravitational waves that may be observed by the Laser Interferometer Space Antenna (LISA). In Paper I of this series, we used the population of ≈2000 galaxy mergers predicted by the TNG50-3 simulation to seed semi-analytic models of the orbital evolution and coalescence of MBH pairs with initial separations of ≈1 kpc. Here, we calculate the dAGN luminosities and separations of these pairs as they evolve in post-merger galaxies, and show how the coalescence fraction of dAGNs changes with redshift. We find that because of the several gigayear-long dynamical friction timescale for orbital evolution, the fraction of dAGNs that eventually end in an MBH merger grows with redshift and exceeds 50% beyond $z_{\rm dAGN} \approx 1$. Dual AGNs in galaxies with bulge masses $\lesssim 10^{10}\ M_{\odot}$, or consisting of near-equal-mass MBHs, evolve more quickly and have higher than average coalescence fractions. At any redshift, dAGNs observed with small separations ($\lesssim$0.7 kpc) have a higher probability of merging before $z = 0$ than more widely separated systems. Radiation feedback effects can significantly reduce the number of MBH mergers, and this could be manifested as a larger than expected number of widely separated dAGNs. We present a method to estimate the MBH coalescence rate as well as the potential LISA detection rate given a survey of dAGNs. Comparing these rates to the eventual LISA measurements will help determine the efficiency of dynamical friction in post-merger galaxies.

*Unified Astronomy Thesaurus concepts:* Galaxies (573); Galaxy evolution (594); Galaxy dynamics (591); Galaxy kinematics (602); Galaxy nuclei (609); Supermassive black holes (1663)

## 1. Introduction

Dual active galactic nuclei (dAGNs) are two accreting massive black holes (MBHs) residing within a single host galaxy and are expected to occur following the merger of two massive galaxies. A population of dAGNs in post-merger galaxies seems to be an unavoidable prediction of hierarchical galaxy formation models (e.g., De Rosa et al. 2019). In some cases, the separation of the two MBHs that make up a dAGN will shrink slowly over time as the orbiting MBHs interact with the gaseous and stellar backgrounds of the galaxy (e.g., Begelman et al. 1980; Volonteri et al. 2003; Barausse 2012; Valiante et al. 2016; Bonetti et al. 2019; Khan et al. 2020; Li et al. 2022), eventually leading to the emission of gravitational waves and the coalescence of the two black holes (e.g., Amaro-Seoane et al. 2017; Kelley et al. 2017, 2019). Therefore, dAGNs are "tracers" of future MBH mergers and gravitational wave events. An observed sample of dAGNs, combined with a model describing their future evolution, can thus provide a prediction of the MBH merger rate, a critical parameter for the upcoming Laser Interferometer Space Antenna (LISA) gravitational wave observatory.

Electromagnetic observations of dual AGNs have been challenging because of the rarity of these objects and the high spatial resolution required to distinguish two sources with kiloparsec separation in astronomical images. Consequently, initial detections of dAGNs identified relatively widely separated pairs (∼1–10 kpc; Komossa et al. 2003; Ballo et al. 2004; Guainazzi et al. 2005; Bianchi et al. 2008; Piconcelli et al. 2010). Several subsequent studies performed systematic searches for dAGNs at low redshift in large IR, optical, and X-ray surveys (Koss et al. 2010; Liu et al. 2011; Comerford et al. 2012; Ricci et al. 2017). Among these, the Sloan Digital Sky Survey (SDSS) has been used to identify dAGNs in the optical part of the spectrum through both imaging (for spatially resolved systems) and spectroscopy (for spatially unresolved systems with double-peaked narrow emission lines; Wang et al. 2009; Smith et al. 2010; Ge et al. 2012; Kim et al. 2020). The spectroscopic searches also encountered a practical challenge stemming from the fact that double-peaked lines are not a unique signature of MBH pairs at kiloparsec separations and are also commonly produced by systems with AGN-driven outflows.

In the near future, radio surveys that have longer baseline arrays at higher frequencies, like the next generation Very Large Array (ngVLA, Burke-Spolaor et al. 2018; Murphy 2018), will come into operation. With its anticipated angular resolution, ngVLA will be able to distinguish gravitationally bound MBH pairs at $z \sim 0.1$ when observing at 10 GHz. New X-ray observatories (e.g., Athena, Nandra et al. 2013) will greatly enlarge the population of known dAGNs with separations of a few tens of kiloparsecs. New mid-infrared observatories (e.g., JWST, Gardner et al. 2006) will

also dramatically increase the population of known dAGNs, especially at separations $\lesssim$1 kpc (De Rosa et al. 2019).

Whether an observable dAGN results in an MBH coalescence depends on the physical processes within the remnant galaxy that drive the orbital evolution of the MBHs. When the MBHs are at separations of ∼1 kpc, dynamical friction (DF) by gas and stars is expected to dominate the orbital decay (Begelman et al. 1980). In this process, gravitational deflection of gas (Ostriker 1999; Kim & Kim 2007) or collisionless particles (e.g., stars and dark matter, Chandrasekhar 1943; Antonini & Merritt 2012) causes an overdense wake to form behind each MBH. The wakes exert a gravitational pull on the MBHs, which saps their orbital energy. Once the two MBHs are gravitationally bound (at separations of a few parsecs) stellar "loss-cone" scattering is expected to dominate the orbital decay (e.g., Quinlan 1996; Quinlan & Hernquist 1997; Yu 2002). If the galaxy is sufficiently gas-rich, drag on the binary by the surrounding circumbinary disk may also affect its orbital evolution at separations $\lesssim$0.1 pc (e.g., Armitage & Natarajan 2005; Milosavljević & Phinney 2005). Only when the separation falls below ∼1000 Schwarzschild radii does gravitational wave emission begin to dominate the orbital evolution until the MBHs merge (e.g., Thorne & Braginskii 1976; Begelman et al. 1980). In addition to the orbital decay, the gas content of the post-merger galaxy will also strongly influence the accretion rates onto the MBHs and their subsequent properties as dAGNs. As a result, connecting observations of dAGNs to their potential future gravitational wave sources will depend on the properties of the host galaxy and the orbit of the MBH pair (e.g., Li et al. 2021).

In Paper I of this series (Li et al. 2022), we presented the results of a semi-analytic model that followed the dynamical evolution of ≈8000 MBH pairs from ∼1 kpc to coalescence, accounting for all the processes described above (DF, loss-cone scattering, decay in a circumbinary disk, and gravitational wave emission). The host galaxy models in which the MBH pairs evolved were constructed from the properties of merger galaxies in the TNG50-3 cosmological simulation (Nelson et al. 2019a, 2019b; Pillepich et al. 2019). Paper I showed that the DF phase was the most important process in determining whether an MBH pair would coalesce within a Hubble time, and therefore the stellar and gas contents at scales of a few hundred parsecs in post-merger galaxies are critical for the expected LISA detection rates.

Here, we build on the results of Paper I by describing the expected dAGN properties of MBH pairs as they evolve toward coalescence. Paper I shows that the galaxy properties at ∼1 kpc scale are often crucial for the overall orbital decay, and so we focus on the dAGN properties with separations in this range. As our model follows these MBH pairs through to coalescence, we demonstrate that observational surveys of dAGNs can provide an estimate of the expected MBH merger rate.

We also explore the effect of radiation feedback on the expected MBH merger rate. Earlier studies have shown the radiation produced by each MBH of a dAGN can influence the dynamics of the system (Kim & Kim 2007; Li et al. 2020a). For MBHs evolving in gas-rich backgrounds, the ionizing radiation emerging from the innermost parts of the MBHs' accretion flows can affect their gaseous DF wake and render gas DF inefficient for a range of physical scenarios. MBHs in this regime tend to experience positive net force, meaning that they speed up, contrary to the expectations for gaseous DF without radiative feedback (Park & Bogdanović 2017; Li et al. 2020a; Gruzinov et al. 2020; Toyouchi et al. 2020), which could severely reduce the number of MBH mergers detected by LISA. It is crucial, therefore, to find a method that can test these predictions, especially the potential role of radiation feedback, and observationally constrain the LISA expectations.

This paper is organized as follows. In Section 2 we provide a brief summary of the main features of the calculation used to evolve the MBHs and how the TNG50-3 simulation data are used as input to the model. Section 3 shows how the distributions of dAGN luminosity and separation change over time. Section 4 presents the merger fraction of dAGNs at different redshifts and how this depends on the properties of the host galaxy and MBH pair. The impact of radiation feedback on these results is shown in Section 5. Finally, we discuss the implications of our findings in Section 6 and conclude in Section 7. We assume a cosmology consistent with that used in the TNG50-3 simulation ($\Omega_{\Lambda,0}=0.6911$, $\Omega_{m,0}=0.3089$, $\Omega_{b,0}=0.0486$, $h=0.6774$) and $t_{\rm Hubble}=14.4$ billion yr.

## 2. Methods

A thorough description of the calculation of the dynamical evolution of MBH pairs and our use of the TNG50-3 simulation data is found in Paper I (Li et al. 2022, see also Li et al. 2020b). We therefore provide a brief summary of the method below before describing how we compute the time-dependent accretion rate and luminosity of each of our model dAGNs.

### 2.1. The Dynamical Evolution of MBH Pairs in TNG50-3 Post-merger Galaxies

We assume that a galaxy merger produces a single remnant, with a stellar bulge and gas disk,[5] which includes the MBH pair. The nonrotating bulge has a mass $M_{\rm sb}$ and follows a coreless power-law density profile (e.g., Binney & Tremaine 2008), which is cut off at twice the half-mass radius of the bulge ($2R_{\rm b,h}$), with the scale parameters proportional to $R_{\rm b,h}$.[6] The primary MBH (pMBH; with mass $M_1$) is fixed at the center of the galaxy. We consider the orbital evolution of a bare, secondary MBH (sMBH; with mass $M_2<M_1$) that is orbiting in the plane of the gas disk. The total mass of the MBH pair is $M_{\rm bin}=M_1+M_2$ and the mass ratio is $q=M_2/M_1$.

The gas fraction of the remnant galaxy is $f_{\rm g}=M_{\rm gd}/(M_{\rm gd}+M_{\rm sb})$, where $M_{\rm gd}$ is the mass of the gas disk within twice the half-mass radius of the gas disk ($2R_{\rm g,h}$). Once $f_{\rm g}$ is set, the gas densities are determined using an exponential profile with a scale radius defined as $2\log(M_1/10^5\,M_\odot)$ kpc (e.g., Binney & Tremaine 2008). As a result, galaxies with a larger pMBH have gas densities that decrease more slowly with radius.[7] The gas disk of each galaxy rotates with a speed drawn from the uniform distribution (0.7–0.9)$v_{\rm c}(r)$, where $v_{\rm c}(r)$ is the local circular velocity.

[5] We neglect the stellar disk in the calculation as its impact on the orbital evolution of an MBH is relatively minor (Li et al. 2020b).

[6] The definition of the bulge scale parameters in Section 2.1 of Paper I is incorrect. In both Paper I and this paper, the bulge scale parameters are proportional to $R_{\rm b,h}$.

[7] The assumption of an exponential profile is commonly used in semi-analytical models of MBH pair evolution. The density profile cannot be extracted from TNG because the resolution limit of TNG50-3 is kiloparsec scale, and we need a density profile of the gas disk below that scale for the estimation of gaseous dynamical friction.

A list of 1997 galaxy merger events, including redshifts and MBH masses, is extracted from the catalogs of the TNG50-3 simulation.[8] Specifically, the redshifts correspond to when the two MBHs reach a separation equal to the gravitational softening length of the collisionless component (≈1 kpc). The properties of the remnant galaxy ($M_{\rm sb}$, $M_{\rm gd}$, $R_{\rm b,h}$, and $R_{\rm g,h}$) are also extracted from the TNG50-3 catalogs and are used to construct the galaxy model within which the MBH pair evolves. The dynamical evolution of the pair is initialized so that the semimajor axis is $a \approx 1$ kpc. The initial eccentricity of the sMBH is set to be either $e_i < 0.2$ or $0.8 \leqslant e_i \leqslant 0.9$, and we consider both prograde and retrograde orbits (Li et al. 2020b). Thus, we compute four distinct evolutions of the sMBH in each of the 1997 post-merger galaxies. The results presented below are from the combined data set of 7988 calculations.

The orbital evolution of the sMBH due to DF is computed as described by Li et al. (2020a, 2020b). This process takes the sMBH down to the influence radius of the MBH pair, where the mass enclosed by the orbit is equal to twice the pair mass. Below this radius, the orbital decay is due to the combination of loss-cone scattering, drag from the circumbinary gas disk, and gravitational wave emission. The calculation ends when the orbital separation is smaller than the radius of the innermost stable circular orbit (ISCO) of a nonspinning MBH pair (i.e., $R_{\rm ISCO} = 6GM_{\rm bin}/c^2$). Paper I provides full details of how the orbital evolution is computed below the influence radius. The full decay time of the sMBH is tracked and the MBH coalescence redshift, $z_{\rm coal}$, is recorded for each calculation that merges within the Hubble time (36% of the 7988 orbital evolutions do not successfully merge within this time; see Section 3 of Paper I).

Lastly, for those models that successfully reach coalescence, we compute the expected LISA signal-to-noise ratio (S/N) during the inspiral phase assuming a four-year mission lifetime (Appendix A of Paper I; Bonetti et al. 2019). The detection threshold for LISA used in this paper is S/N > 8. This information will allow us to connect LISA-detectable MBH pairs to their earlier dAGN properties.

### 2.2. Accretion Rates and Luminosities

The accretion rates onto both the pMBH and sMBH are calculated as a function of time during the DF phase of the calculation. That is, we compute the dAGN luminosities only when the separations are greater than the influence radius of the MBH pair (∼1 pc). We do not model the luminosity of dual AGNs when their separation is smaller than 1 pc, because our model does not capture accretion onto gravitationally bound MBH pairs. The evolution time of MBH pairs from 1 pc to coalescence is much shorter than the evolution time from kiloparsec scale to 1 pc (as shown in Figure 1 of Li et al. 2020b). As a result, the contribution to mean luminosity of the subparsec phase of the MBH pair evolution is negligible. For simplicity, we neglect the increase in mass of each MBH due to accretion and consider only bolometric luminosities (see Section 6).

The accretion rate onto the stationary pMBH is computed using the Bondi formula (Bondi & Hoyle 1944; Bondi 1952) and its luminosity is limited to be no more than 10% of the Eddington luminosity (e.g., Lusso et al. 2012), i.e.,

$$L_1 = \begin{cases} 0.1\dot{M}_{\rm B1}c^2 & \text{when} \quad L_1 < 0.1L_{\rm 1,Edd}, \\ 0.1L_{\rm 1,Edd} & \text{otherwise}, \end{cases} \tag{1}$$

where $\dot{M}_{\rm B1} = \pi\, n_{\rm gd0}\, m_{\rm p} (GM_1)^2/c_{\rm s1,\infty}^3$ is the Bondi accretion rate onto the pMBH and $L_{\rm 1,Edd} = 4\pi GM_1 m_{\rm p} c/\sigma_{\rm T}$ is its Eddington luminosity. In the Bondi formula $n_{\rm gd0}$ is the central gas density and $c_{\rm s1,\infty}$ is the sound speed at the galactic center. To determine the sound speed, the temperature profile of the gas disk is assumed to be $10^4$ K above the minimum Toomre stability temperature (Toomre 1964).

As the sMBH is moving through the post-merger galaxy, its accretion rate is calculated using the Bondi–Hoyle–Lyttleton model, which accounts for the drop in accretion due to the relative motion of the MBH (Hoyle & Lyttleton 1939; Bondi & Hoyle 1944; Bondi 1952), $\dot{M}_{\rm BHL} = \dot{M}_{\rm B2}/(1 + \Delta v^2/c_{\rm s2,\infty}^2)^{3/2}$. Here, $\dot{M}_{\rm B2}$ represents the regular Bondi rate of the sMBH, $c_{\rm s2,\infty}$ is the sound speed of the gas at the same radius as the sMBH, and $\Delta v$ is the velocity of the sMBH relative to the gas disk. The resulting accretion luminosity of the sMBH is

$$L_2 = \begin{cases} 0.1\dot{M}_{\rm BHL}c^2 & \text{when} \quad L_2 < L_{\rm 2,\,Edd}, \\ L_{\rm 2,\,Edd} & \text{otherwise}, \end{cases} \tag{2}$$

where $L_{\rm 2,\,Edd} = 4\pi GM_2 m_{\rm p} c/\sigma_{\rm T}$ is the Eddington luminosity of the sMBH.

The dependence of $L_2$ on both gas density and relative velocity means that the AGN luminosity of the sMBH may vary significantly during each orbit and will also show a long-term evolution as the orbit decays. Therefore, we expect the properties of the dAGN population to change with redshift as MBH pairs evolve in time (see also Li et al. 2021). In this paper, we do not consider the instantaneous luminosity of dAGNs; instead, we use the evolution time-weighted luminosity, which is calculated by summing the product of the instantaneous luminosity and the time step through the entire evolution, and then divide it by total evolution time. We find that the radiation feedback does not affect the accretion rate and luminosity of most pMBHs in our models, because the gas densities surrounding them are sufficiently high to counter the effect of the radiation pressure. This places most pMBHs in our model in the so-called hyper-Eddington accretion regime (Inayoshi et al. 2016), characterized by Bondi mass accretion rates larger than the Eddington rate and emergent luminosities $\lesssim L_{\rm Edd}$, limited by photon trapping in the high-density gas (Jiang et al. 2019). Hence, we limit the luminosity of the pMBHs in this regime to 10% of the Eddington luminosity.

The luminosity used in this work to describe both AGNs is the rest-frame bolometric luminosity, with no correction for extinction or host galaxy contamination. We characterize the dAGN luminosity as the sum of the two bolometric luminosities (similar to Volonteri et al. 2022, and other works in the literature) to provide a scale for the luminosity of the system.[9] We defer a careful analysis of the spectral properties

[8] See https://www.tng-project.org/data/docs/specifications.

[9] A survey of dAGNs must resolve the less luminous component of the pair in order to identify the system as a dAGN. This can significantly increase the sensitivity required to detect dAGN pairs. Since the luminosity ratio of the two AGNs in our model varies by 2–4 orders of magnitude during the MBH pair evolution, depending on the properties of the orbits and host galaxy (Li et al. 2021), we simplify our analysis by focusing on the sum of the two luminosities as a means of measuring the scale of the dAGN luminosity.

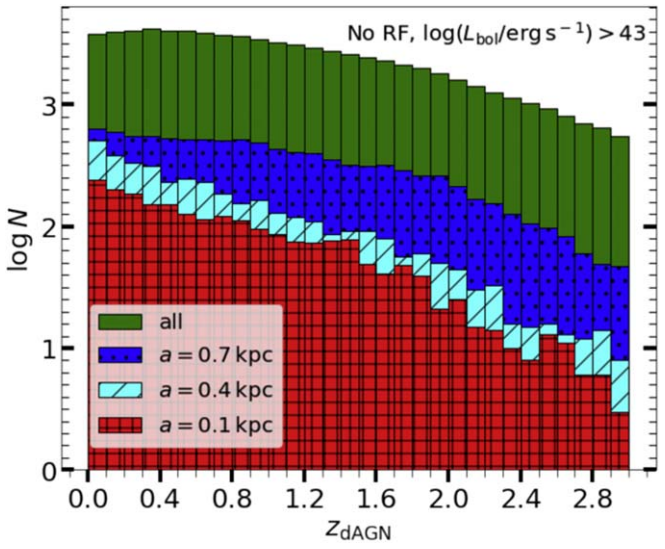


**Figure 1.** The redshift distribution of all dAGNs with total bolometric luminosity larger than $10^{43}$ erg s$^{-1}$ and with separations of 0.7, 0.4, and 0.1 kpc.

of the two AGNs, and strategies to best detect them, to future work.

In the rest of the paper, we explore the connections between dAGNs and MBH merger events. To do so, we define $z_{\rm dAGN}$ as the redshift at which a dAGN is observed and $z_{\rm coal}$ as the redshift at which the two MBHs that comprise the dAGN eventually coalesce (where $z_{\rm coal} < z_{\rm dAGN}$). The luminosity of a dAGN is defined as $L_{\rm bol} = L_1 + L_2$.

## 3. The Evolution of the Luminosities and Separations of Dual Active Galactic Nuclei

In this section we provide an overview of the evolving dAGN population found in our model suite. TNG50-3 predicts a small number of galaxy mergers beyond a redshift of 3 (Figure 2 in Paper I), so we limit our analysis of dAGNs to lower redshifts (in particular, $z_{\rm dAGN} \leqslant 2$) where the population of dAGNs is largest.

The total dAGN bolometric luminosity is the sum of the luminosities of the pMBH and sMBH. As we note in Section 2.2, most of our pMBHs have the bolometric luminosity capped at 10% of the Eddington luminosity. Since the smallest MBHs in our model have mass of $10^6\ M_\odot$, this implies that the luminosity of the MBH pairs in our work is expected to be $>10^{43}$ erg s$^{-1}$. The solid green histogram in Figure 1 shows how the total population of model dAGNs with $L_{\rm bol} > 10^{43}$ erg s$^{-1}$ evolves with $z_{\rm dAGN}$. Since the orbital evolution time of a dAGN in the DF phase is frequently >1 Gyr (Paper I), one system can appear in multiple redshift bins as long as it has $L_{\rm bol} > 10^{43}$ erg s$^{-1}$ in that redshift range. We find that the largest number of dAGNs are present in the redshift range 0.4–0.5, and the number drops as the redshift increases from 0.5 to 3. The distribution of DF evolution times and galaxy gas fractions combine to determine this redshift distribution. Paper I showed that the evolution time for an sMBH to reach $a \sim 0.001$ kpc from $a \sim 1$ kpc ranges from ∼1 Gyr (if the stellar bulge dominates) to ∼5–10 Gyr (if the gas disk dominates) depending on the orbital configuration of the sMBH. Thus, only those systems containing dAGNs whose orbital evolution is determined by stellar DF in the bulge and which have relatively short evolution time will evolve to parsec scales at high $z_{\rm dAGN}$. The dAGNs whose orbital evolution is determined by the slower gaseous DF process reach this separation at lower redshifts.

Figure 1 also illustrates the redshift distribution of dAGNs with separations of 0.7, 0.4, and 0.1 kpc.[10] All three distributions peak at the smallest redshifts $z_{\rm dAGN} \approx$ 0–0.1, but the peak is flattest and the total number of dAGNs highest for $a = 0.7$ kpc. This is because there are always more dAGNs with large rather than small separations. This happens because all dAGNs with small separations were once dAGNs with large separations in the past, but not all dAGNs with large separations evolve into dAGNs with small separations. Taking everything into account, the shape of the redshift distribution of dAGNs is a natural result of DF-dominated orbital evolution. This slow evolution means that $z_{\rm dAGN} \lesssim 0.5$ is the optimal region for observational searches for dAGNs.

Turning now to the 65% of dAGNs that eventually lead to an MBH merger, Figure 2 shows the separation and luminosity distributions at $z_{\rm dAGN} = 0.1$, 1, and 2 of all dAGNs that will coalesce (solid blue histograms). The total number of dAGNs at $z_{\rm dAGN} = 1$ and 2 that eventually merge is larger than that at $z_{\rm dAGN} = 0.1$ because MBH mergers can happen between $z_{\rm dAGN} = 1$ and 0.1 and these do not appear in the leftmost distribution. Note, however, that although the number of dAGNs is larger at high redshift, they are less likely to be observed due to their large luminosity distances. The top three panels of Figure 2 show that most dAGNs at $z_{\rm dAGN} = 1$ and 2 that eventually merge have separations in the range 0.5–1 kpc. This is because the evolution time from ∼1 kpc to coalescence is often in the range 5–10 Gyr (Paper I). The separation distribution at $z_{\rm dAGN} = 2$ (the rightmost panel) has a secondary peak at $a \sim 1.2$ kpc. This is because the time between $z_{\rm dAGN} = 2$ and 0 (≈10 Gyr) is long enough to allow some MBH pairs with separations larger than 1 kpc to merge within a Hubble time. The peak of the distribution at $z_{\rm dAGN} = 0.1$ is shifted toward 0.2–0.5 kpc due to the relatively short evolution time between $z_{\rm dAGN} = 0.1$ and 0 (∼1 Gyr).

The solid blue histograms in the bottom three panels of Figure 2 show the distribution of $L_{\rm bol}$ for all dAGNs at $z_{\rm dAGN} = 0.1$, 1, and 2 whose MBHs merge before $z = 0$. As expected, there is a sharp cutoff at $L_{\rm bol} \approx 10^{43}$ erg s$^{-1}$ due to the minimum MBH mass in the TNG50-3 simulation. At all $z_{\rm dAGN}$ the majority of dAGNs that eventually merge have $L_{\rm bol} \approx 10^{43-45}$ erg s$^{-1}$.

The hatched red histograms in Figure 2 show the distributions of dAGNs that lead to LISA S/N > 8. These potential LISA sources follow a similar trend in the separation distribution at all three redshifts. However, at luminosities larger than $\approx 10^{45}$ erg s$^{-1}$, the fraction of LISA sources drops significantly in the lower three panels. This is because the bolometric luminosity is proportional to the binary mass, so more luminous precursor dAGNs have more massive MBHs and are less likely to be detected by LISA.

## 4. The Coalescence Fraction of Kiloparsec Scale Dual Active Galactic Nuclei

This section presents the coalescence fraction of dAGNs as a function of redshift and observable properties of dAGN hosts. These fractions provide a quantitative relation between the

[10] The separation used in this paper is the physical distance between the two MBHs and not a projected distance on the sky. For a random distribution of dAGN orientations on the sky, the average projected separation is $(\pi/4)$ $a \approx 0.79a$. This value is found by averaging the projected separation ($a \sin(\phi)$, where $\phi$ is the polar angle and the observer is along the $z$-axis) over a hemisphere.

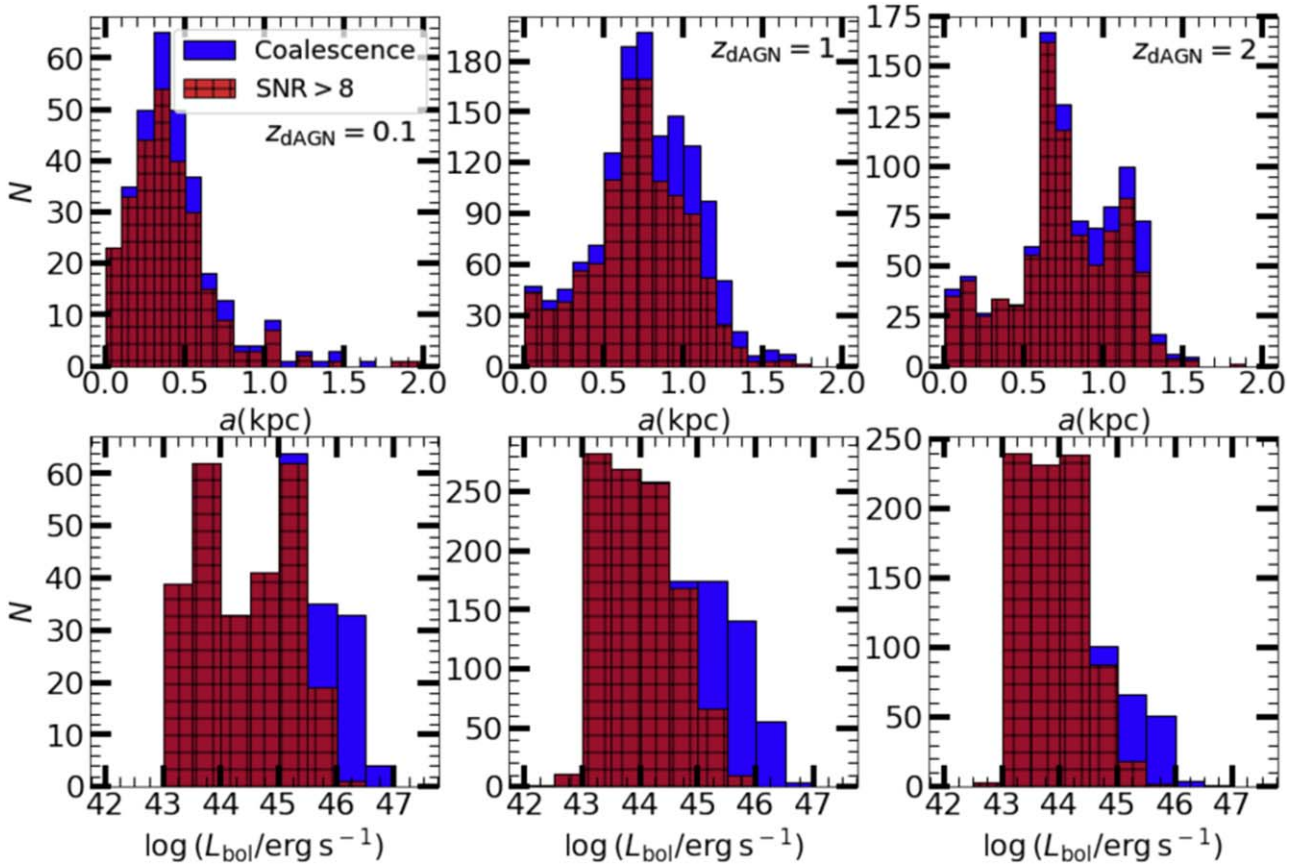


**Figure 2.** The separation and luminosity distributions at $z_{dAGN} = 0.1$, 1, and 2 of dAGNs whose MBHs coalesce by $z = 0$. The blue solid histograms show all dAGNs that eventually lead to coalescence by $z = 0$, and the red hatched histograms show the systems in which the MBH merger has a LISA S/N > 8.

numbers of dAGNs and merging MBHs, and can be used to estimate the cosmological MBH binary coalescence rate and the number of LISA detections from a sample of detected dAGNs.

### 4.1. The Coalescence Fraction as a Function of Dual AGN Redshift

In order to quantify the relationship between observable dAGNs and MBH coalescence, we count the number of dAGNs with $L_{bol} > 10^{43}$ erg s$^{-1}$ with MBHs that coalesce before $z = 0$ and show the coalescence fraction as a function of $z_{dAGN}$ in the left panel of Figure 3, grouped by dAGN separation. Almost all dAGNs with $a = 0.1$ kpc at $z_{dAGN} > 0.1$ eventually coalesce by $z = 0$. The evolution time of these systems is $10^{5-8}$ yr (Paper I), which is sufficient for a dAGN with a separation of $a = 0.1$ kpc at $z_{dAGN} = 0.1$ to coalesce (the corresponding cosmological time is ∼1.3 Gyr). Thus, if a dAGN is observed with $a \leqslant 0.1$ kpc at any redshift larger than 0.1, then it has nearly 100% chance to coalesce before $z = 0$.

Similarly, all dAGNs with $a = 0.4$ kpc at $z_{dAGN} > 0.4$ coalesce before $z = 0$, but the coalescence fraction between $z_{dAGN} = 0$ and 0.1 drops to ∼0.3, showing that the majority of these systems have an evolution time longer than ∼1.3 Gyr. The coalescence fraction of dAGNs with separations of 0.7 kpc gradually increases as redshift grows. This is as expected, since higher-redshift dAGNs that reach separations of $a = 0.7$ kpc have a greater probability to evolve to coalescence prior to $z = 0$. Indeed, Figure 3 shows that nearly 90% of dAGNs with $a = 0.7$ kpc at $z_{dAGN} = 3$ lead to an MBH merger. However, this fraction drops to 50% at $z_{dAGN} = 0.3$. The coalescence fraction of dAGNs with separations of

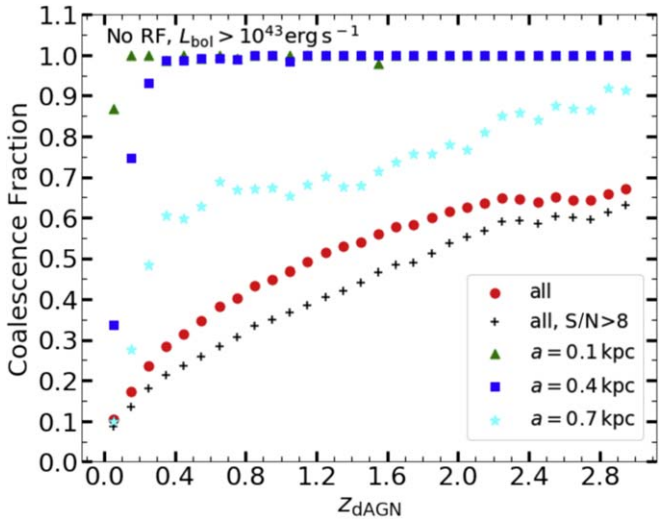


**Figure 3.** The fraction of dAGNs observed at a given redshift whose MBHs coalesce before $z = 0$. The red circles show the fraction using all 7988 dAGNs in the model suite, while the green triangles, blue squares, and cyan stars show how the fraction varies with dAGN separation. The black "+" symbols indicate the fraction of all dAGNs that lead to a LISA S/N > 8.

$a = 0.7$ kpc is in general lower than for those with $a = 0.1$ or 0.4 kpc because it is easier for the sMBH to evolve to coalescence from 0.1 kpc than from 0.7 kpc.

The coalescence fraction of all dAGNs with $L_{bol} > 10^{43}$ erg s$^{-1}$ is shown as the red circles in Figure 3 and is ∼70% at $z_{dAGN} = 3$ and ∼50% at $z_{dAGN} = 1$. Thus, given a

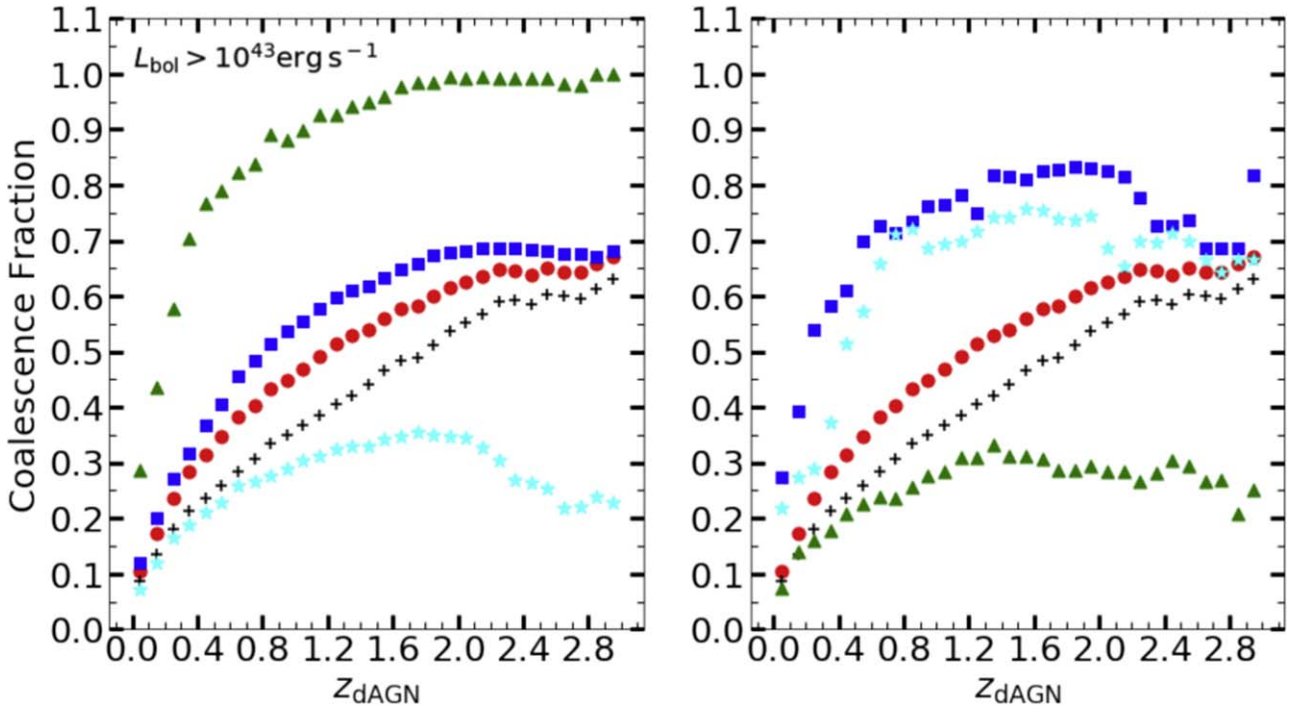


**Figure 4.** The fraction of dAGNs at a given redshift that coalesce by $z = 0$. Left: the coalescence fraction of dAGNs grouped by the bulge mass. Green triangles represent systems with $\log(M_{sb}/M_{\odot}) = 9$, blue squares represent systems with $\log(M_{sb}/M_{\odot}) = 10$, and cyan stars represent systems with $\log(M_{sb}/M_{\odot}) = 11$. Right: the coalescence fraction of dAGNs grouped by $\log q$. Green triangles represent systems with $\log q = -2$, blue squares represent systems with $\log q = -1$, and cyan stars represent systems with $\log q = -0.3$. In both panels, red circles illustrate the coalescence fraction of all dAGNs, and the black plus signs represent the fraction of all dAGNs that coalesce by $z = 0$ and can be detected by LISA.

sample of $z_{dAGN} = 1$ dAGNs with $L_{bol} > 10^{43}$ erg s$^{-1}$ with separations of 0.001–2 kpc, we expect that half of them will coalesce before $z = 0$. In order to estimate the number of potential LISA sources using the number of observed dAGNs, we also count the number of dAGNs that coalesce before $z = 0$ with LISA S/N $> 8$ and show this fraction as black plus signs in Figure 3. As expected, the LISA-detectable fraction is lower than the coalescence fraction at all redshifts, since LISA will not be as sensitive to the most massive MBH pairs.

Since the evolution time of the sMBH depends on the properties of the post-merger galaxy and MBH pair (Li et al. 2022, Paper I), Figure 4 shows how the coalescence fraction of dAGNs is impacted by the bulge mass of the galaxy (left panel) and the MBH binary mass ratio (right panel). We find that the coalescence fraction of dual AGNs is inversely proportional to $M_{sb}$, with the largest fractions in galaxies with bulge masses of $M_{sb} \approx 10^9\ M_{\odot}$ and the lowest with $M_{sb} \approx 10^{11}\ M_{\odot}$. This is a result of the inverse relationship between $M_{sb}$ and $f_g$ (Section 2.1), so that galaxy models with less massive bulges have higher gas fractions (and thus high gas densities and sound speeds), where gaseous DF efficiently decays the orbit of the sMBH at large separations (see also Paper I).[11] When $M_{sb} > 10^{10}\ M_{\odot}$, the gas fraction falls to low enough values that gaseous DF becomes inefficient, increasing the decay time of the sMBH before the stellar DF can take over. The coalescence fractions of the entire dAGN population (red circles) and the population that leads to LISA S/N $> 8$ (black plus signs) closely follow the results for $M_{sb} = 10^{10}\ M_{\odot}$. This illustrates that galaxies with $M_{sb} \approx 10^{10}\ M_{\odot}$ dominate the sample of post-merger galaxies in TNG50-3. The right panel of Figure 4 shows that the coalescence fractions of dAGNs with $\log q = -1$ and $-0.3$ are the highest because the DF forces are larger (and the inspiral time shorter) for higher-mass sMBHs (Li et al. 2020b, their Figure 11).

### 4.2. The Cumulative Coalescence Fractions of Dual AGNs

The results above focused on dAGNs that evolve to an MBH merger before $z = 0$, but it is also interesting to examine how these mergers are distributed across redshift $z_{coal}$. Figure 5 shows the cumulative coalescence fractions (CCFs) of dAGNs with $L_{bol} > 10^{43}$ erg s$^{-1}$ at $z_{dAGN} = 1$, 2, and 3.

The three lines in each panel shows the CCFs for dAGNs with different separations at the starting $z_{dAGN}$. Unsurprisingly, we see that dAGNs that start with a separation of only $a = 0.1$ kpc evolve to coalescence efficiently, reaching a 100% coalescence fraction by $z \approx 0.9$, 1.8, and 2.6, if starting at $z_{dAGN} = 1$, 2, and 3, respectively. Similarly, 100% of the dAGNs with $a = 0.4$ kpc in our sample that are at $z_{dAGN} = 2$ or 3 merge by $z \approx 1.2$ and 2.2. Our calculations suggest that there may still be a small fraction of the $z_{dAGN} = 1$, $a = 0.4$ kpc population at low $z$, but the majority of them would have merged by $z \approx 0.8$. In contrast, Figure 5 shows that dAGNs with separations of $a = 0.7$ kpc at $z_{dAGN} = 1$ or 2 will not all have merged by $z = 0$ although the ones starting at $z_{dAGN} = 3$ would all have merged by $z \approx 0.4$. Of course, the dAGNs that remain at low redshifts will be at significantly smaller separations (e.g., Figure 2).

[11] For a dAGN to have a bolometric luminosity larger than $10^{43}$ erg s$^{-1}$, the gas density around the pMBH and sMBH needs to be larger than a certain threshold, which basically sets a threshold for the gas mass in the host galaxy. In TNG, lower-mass galaxies have larger gas fractions on average, so the gas fraction of a dAGN in a $10^9\ M_{\odot}$ bulge is larger than that in a $10^{11}\ M_{\odot}$ bulge on average, if these two dAGNs have similar bolometric luminosities. According to Figure 3 in Li et al. (2022), the coalescence fraction of TNG50-3 MBHBs in systems with high gas fractions is much larger than that in systems with low gas fractions, which explains this trend in bulge mass.

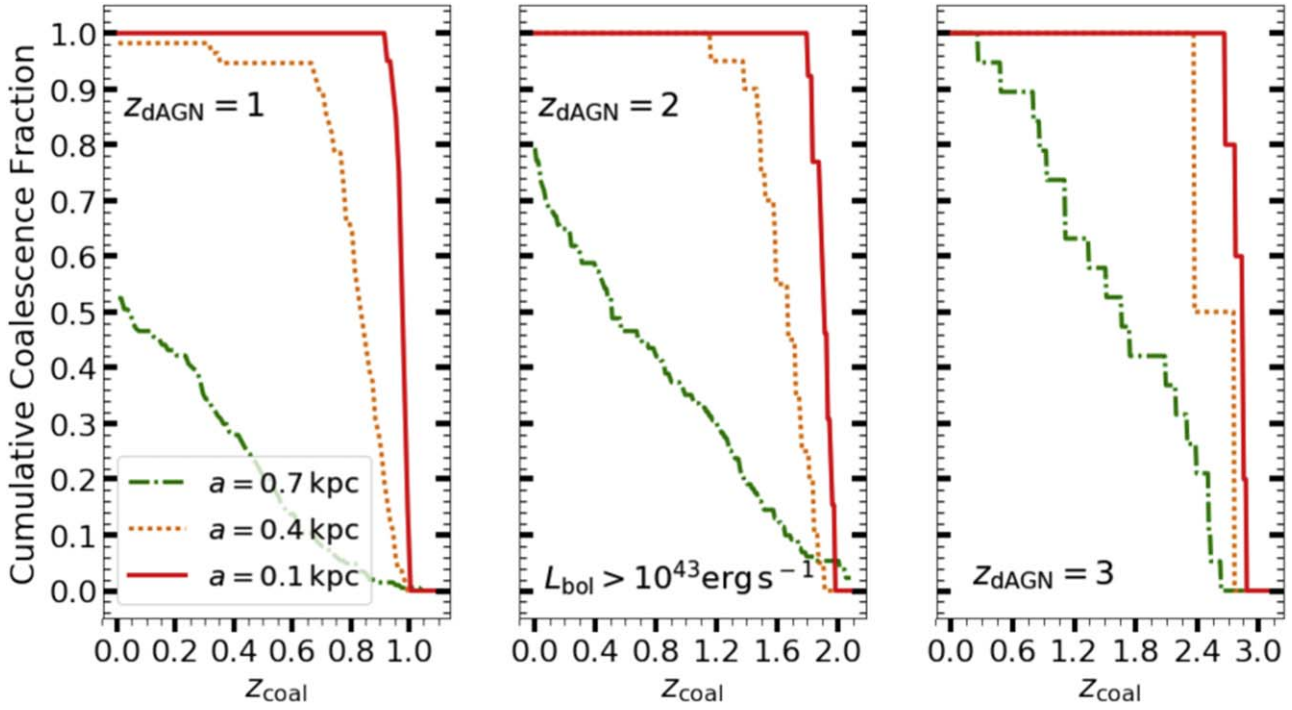


**Figure 5.** The cumulative coalescence fractions of dAGNs with $L_{bol} > 10^{43}$ erg s$^{-1}$ at $z_{dAGN} = 1$, 2, and 3. The dotted–dashed green lines show the CCFs of dAGNs with separations of $a = 0.7$ kpc, while the dotted orange lines and solid red lines represent dAGNs with separations of 0.4 and 0.1 kpc, respectively.

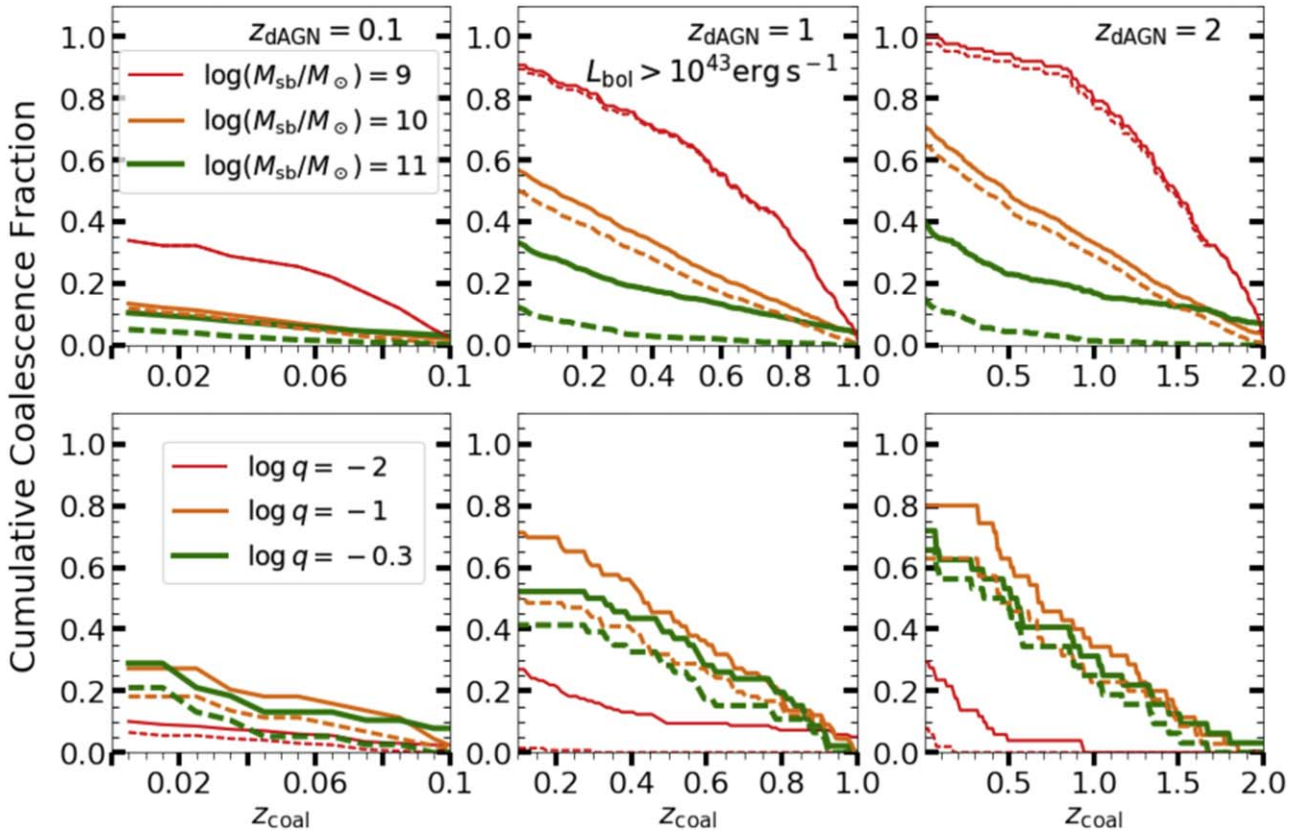


**Figure 6.** The cumulative coalescence fractions of dAGNs at $z_{dAGN} = 0.1$, 1, and 2 with $L_{bol} > 10^{43}$ erg s$^{-1}$ grouped by the stellar bulge mass (top row) and the MBH mass ratio (bottom row). The dashed lines show the CCFs of mergers that result in LISA events with S/N > 8.

As in Figure 4, we show in Figure 6 how the CCFs vary with $\log M_{sb}$ (upper panels) and $\log q$ (lower panels). Dual AGNs of all separations are included in each curve, and the dashed lines show CCFs of those mergers with LISA S/N > 8. We replace the $z_{dAGN} = 3$ panels with one at $z_{dAGN} = 0.1$ to more closely connect to observational searches for dAGNs.

In the upper row of the figure, we see the same inverse relationship between $M_{sb}$ and coalescence fractions as seen in Figure 4. For example, ~30%–40% of $z_{dAGN} = 0.1$ dAGNs in galaxies with $M_{sb} = 10^9\ M_\odot$ bulges will have coalesced by $z = 0$. However, if the dAGNs reside in post-merger galaxies with $M_{sb} > 10^{10}\ M_\odot$, then only ~10% will merge before $z = 0$. The fractions increase markedly when considering dual AGNs at higher redshifts; however, the fraction never rises above 40% for dAGNs in the most massive bulges. In the bottom row of Figure 6, we again see that MBH pairs with larger values of $\log q$ will evolve faster and reach coalescence at higher redshift than those with lower values of $\log q$. The implication of this is that the most likely population of dAGNs persisting to low redshift will be systems with $\log q \lesssim -2$ and in galaxies with $\log M_{sb} \gtrsim 11\ M_\odot$. Conversely, as shown by the dashed lines, the largest fraction of LISA detections will originate from MBH pairs evolving in lower-mass bulges (see also Paper I).

## 5. The Impact of Radiation Feedback Effects

The thermal pressure of the ionized bubble surrounding an accreting MBH regulates its accretion rate (e.g., Ostriker et al. 1976; Begelman 1985; Ricotti et al. 2008; Park & Ricotti 2011, 2012) and suppresses its luminosity. The magnitude of this effect depends on the motion of the MBH relative to its gas environment, the gas density, and the temperature of surrounding gas (Park & Ricotti 2013). Meanwhile, the ionized bubble can also reduce the DF force on MBHs moving in gas-rich hosts (Park & Bogdanović 2017; Gruzinov et al. 2020; Toyouchi et al. 2020), an effect known as "negative DF." In several previous papers we showed that these radiation feedback (RF) effects may impact both the dAGN luminosities and the overall dynamical evolution of the sMBH (Li et al. 2022, Paper I). In particular, Paper I showed that the negative DF effect increases the orbital decay timescale of sMBHs in gas-rich hosts, which could, in principle, severely reduce the expected LISA detection rates. In this section, we explore how RF will impact the evolution of the dAGN population. As the reduction in $L_{bol}$ is relatively modest (RF does not typically impact the luminosity of the pMBH; Li et al. 2021), we focus here on the RF effects on the orbital decay of the sMBH. Details on how we implement RF in the calculation of the DF force can be found in the paper by Li et al. (2020a). We note that the RF effects are only computed during the DF phase of the MBH evolution, but, as seen Paper I, this phase dominates the overall timescale of an MBH merger.

Figure 7 shows the redshift distribution of all dAGNs in our model suite with $L_{bol} > 10^{43}$ erg s$^{-1}$ when the RF effects are included in the calculations. This plot should be compared to Figure 1, which shows the results in the absence of RF. The green histogram shows the redshift distribution of all dAGNs and is similar to the one in Figure 1, except that there are more dAGNs at $z \approx 0$–0.4 when RF effects are included. This is because negative DF slows the orbital decay, which results in longer evolution time and more dAGNs at low redshifts. Figure 7 also illustrates the redshift distribution of dAGNs with separations of $a = 0.7$, 0.4, and 0.1 kpc in the presence of RF. dAGNs separated by $a = 0.7$ kpc still dominate the population as in Figure 1. However, when RF effects are included there are fewer dAGNs with separations of 0.4 and 0.1 kpc, especially at large redshifts. This is because negative DF increases the evolution time of most systems with gas fractions larger than 0.1 (Li et al. 2020a). Thus, it takes longer for most systems to

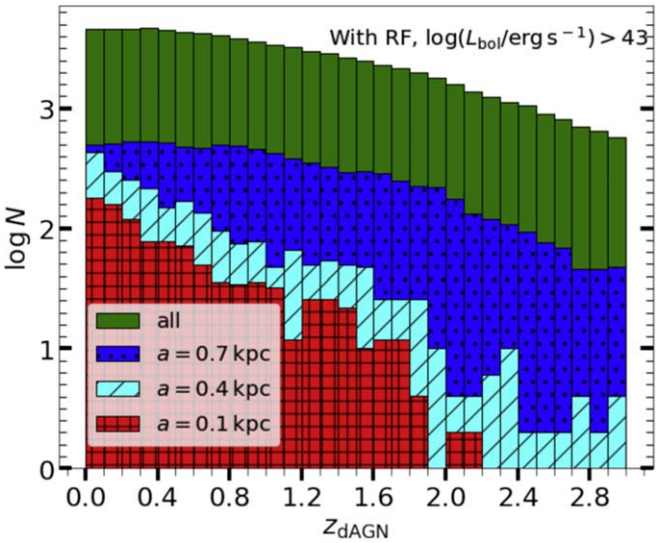


**Figure 7.** As Figure 1, but now showing the redshift distributions when including the effects of radiation feedback.

reach smaller separations in the presence of RF, and thus there are fewer dAGNs with separations <0.4 kpc at high redshifts when RF is taken into account.

The impact of RF on the separation and luminosity distributions of all dAGNs that evolve to coalescence is shown in Figure 8 and should be compared to Figure 2. Critically, the total number of systems that reach coalescence decreases in all panels when RF effects are included, with the largest drop when $z_{dAGN} = 2$. This is a result of the increase in evolution time caused by RF effects (see Paper I). The shapes of the separation distributions are largely similar in the two cases except for the one at $z_{dAGN} = 2$, which remains bimodal in the presence of RF, but the left peak at $a = 0.6$–0.7 kpc is now lower than the right peak at $a = 1.2$–1.3 kpc, contrary to the outcome in the absence of RF. This is because the left peak is dominated by lower-mass gas-rich systems, which are more affected by RF than the more massive systems in the right peak.

The right peak at $a = 1.2$–1.3 kpc is largely due to dAGNs whose orbital evolution is determined by stellar DF in the bulge, which are also the ones that are least affected by RF, so the right peak is only slightly reduced in the presence of RF.

The bottom row of Figure 8 shows the bolometric luminosity distribution of all dAGNs that eventually coalesce in the presence of RF. Comparing this bottom row to the one in Figure 2, we find that most dAGNs that evolve to mergers continue to have $L_{bol} = 10^{43-44}$ erg s$^{-1}$ at all $z_{dAGN}$ in the presence of RF, but the total number of such systems has decreased significantly. However, the peak at $L_{bol} = 10^{45-46}$ erg s$^{-1}$ is barely affected by RF. This is because $L_{bol}$ is proportional to the MBH pair mass, so the higher luminosity peak is composed of more massive dAGNs whose orbital evolution is determined by stellar DF in the bulge and is least affected by RF. Thus, the more luminous dAGNs are barely affected by RF. The red hatched histograms indicate systems that evolve to MBH mergers with LISA S/N > 8. As these mergers are concentrated in the systems with lower mass and lower $L_{bol}$, RF effects significantly decrease the number of these events (see also Paper I).

The impact of RF on the evolution of dAGNs is clearly seen in Figure 9, which shows the coalescence fraction of dAGNs with $L_{bol} > 10^{43}$ erg s$^{-1}$ as a function of $z_{dAGN}$. Almost all dAGNs with separations of $a = 0.1$ kpc at $z_{dAGN} > 0.1$ coalesce before $z = 0$,

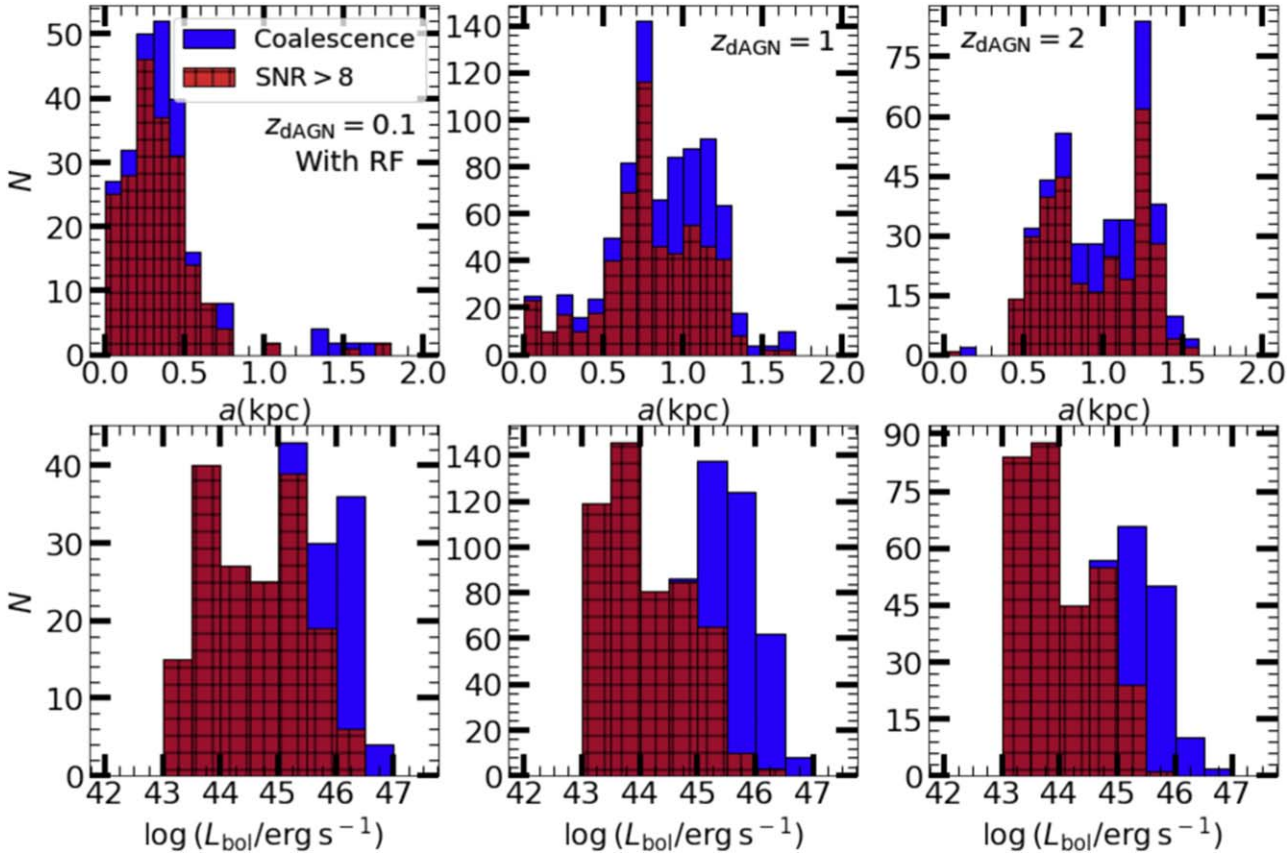


**Figure 8.** As Figure 2, but now showing the separation and luminosity distributions when RF effects are included.

similar to the case in the absence of RF (Figure 3). However, there are no $a = 0.1$ kpc data points at $z_{dAGN} > 1.8$, since negative DF increases the evolution time, and none of our systems reaches $a = 0.1$ kpc at these redshifts. The square and star markers show the coalescence fractions of dAGNs with $a = 0.4$ and 0.7 kpc, respectively. Comparing to the coalescence fractions in the absence of RF as shown in Figure 3, at $z_{dAGN} < 1.8$, the coalescence fractions are in general reduced by 10%–20% for $a = 0.4$ kpc dAGNs in the presence of RF, while for $a = 0.7$ kpc dAGNs the coalescence fraction is reduced by 30%–50%. At $z_{dAGN} > 1.8$, the coalescence fractions are reduced significantly to 0.2–0.3 whatever the dAGN separation.

Lastly, the red circles in Figure 9 represent the coalescence fraction of all dAGNs with $L_{bol} > 10^{43}$ erg s$^{-1}$ in the presence of RF. The coalescence fraction at $z_{dAGN} > 0.7$ is nearly flat, and corresponds to 0.2–0.25. Thus, in the presence of RF, if dAGNs are observed at $z_{dAGN} > 0.7$, then we expect 20%–25% of them to coalesce by $z = 0$. The black plus signs in this plot illustrate the fraction of LISA gravitational wave sources in the presence of RF. Similar to the case in the absence of RF, the LISA-detectable fraction of dAGNs is in general ∼5%–10% lower than the total coalescence fraction.

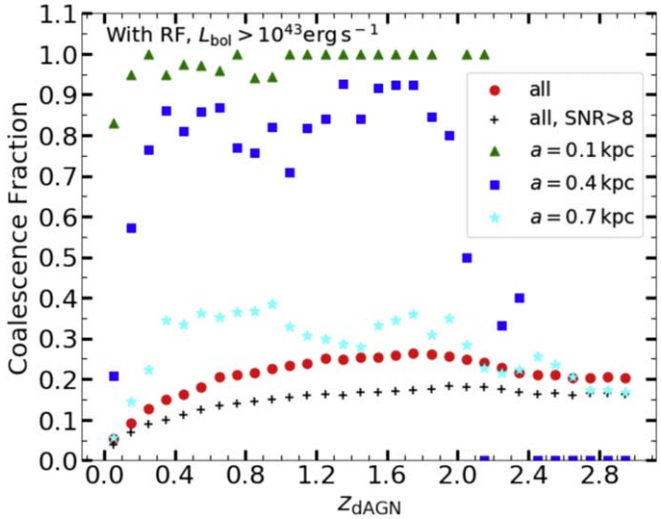


**Figure 9.** Same as Figure 3 but for the scenario when the effects of radiation feedback are taken into account. The red circles show the fraction using all dAGNs in the model suite, while the green triangles, blue squares, and cyan stars show how the fraction varies with dAGN separations of 0.1, 0.4, and 0.7 kpc. The black "+" symbols indicate the fraction of all dAGNs that lead to a LISA S/N > 8 in the presence of RF.

## 6. Discussion

### 6.1. Predicting the MBH Merger Rate from Dual AGN Observations

The results presented above allow an estimate of the MBH merger rate, and the subsequent LISA detection rate, to be derived from an observational survey of kiloparsec-scale dAGNs. Predictions can be calculated either in the presence or in the absence of RF effects. Given a survey of dAGNs with $L_{bol} > 10^{43}$ erg s$^{-1}$ at $z_{dAGN} \pm \Delta z$, the rate at which the MBHs in these systems merge before $z = 0$ is

$$\frac{dN_{coal}}{dt}(z_{dAGN}) = f_{coal}\, n\, \frac{4\pi c d_L^2}{(1 + z_{dAGN})^2}, \quad (3)$$

where $f_{\rm coal}$ is the coalescence fraction at $z_{\rm dAGN}$ from Figure 3, $d_L$ is the luminosity distance to $z_{\rm dAGN}$, and $n$ is the observed dAGN comoving number density at $z_{\rm dAGN}$. In reality, the electromagnetic surveys will not recover all kiloparsec-scale dAGNs at a given redshift because some cannot be spatially resolved due to the projection effects. The obscuration may also "hide" a number of dAGNs from view. This will result in a lower inferred comoving number density of dAGNs and lower merger rates derived from observations.

As an example, consider a future all-sky survey that detects $N$ kiloparsec-scale dAGNs with $L_{\rm bol} > 10^{43}$ erg s$^{-1}$ at $z_{\rm dAGN} = 1 \pm 0.01$. Then

1. the dAGN comoving number density is $n = N/4\pi d_L^2 cdt$. The time interval $dt$ is the cosmological time across $z_{\rm dAGN} = 1 \pm 0.01$, which is 0.081 Gyr in our adopted cosmology (see Section 1).
2. According to Figure 3 the coalescence rate for dAGNs at $z_{\rm dAGN} = 1$ in the absence of RF effects is $f_{\rm coal} \approx 0.45$. The fraction of dAGNs that lead to a merger with a LISA S/N > 8 is ≈0.35.
3. The coalescence rate of these dAGNs at $z_{\rm dAGN} = 1$ is found from Equation (3): $dN_{\rm coal}/dt \sim 1.4 \times 10^{-9} N$ yr$^{-1}$. The rate of mergers with a LISA S/N > 8 is $\sim 1.1 \times 10^{-9} N$ yr$^{-1}$.

To include the effects of RF, the calculation can be repeated using the values of $f_{\rm coal}$ from Figure 9. In the example above, RF reduces the predicted merger rates to $0.77 \times 10^{-9} N$ yr$^{-1}$ (all systems) and $0.46 \times 10^{-9} N$ yr$^{-1}$ (those with LISA S/N > 8).

Equation (3) gives the expected rate of MBH mergers from a population of dAGNs at a particular $z_{\rm dAGN}$. If this estimate can be made for multiple redshifts, the results can be integrated to yield the total MBH merger rate. In Paper I we found that the overall MBH coalescence rate is ∼0.45 yr$^{-1}$ in the absence of RF effects, while the rate of sources with a LISA S/N > 8 is ∼0.34 yr$^{-1}$. Comparing the merger rates derived from dAGN observations and Equation (3) with future LISA measurements will provide important constraints on the efficiency of DF forces and RF effects in the orbital evolution of MBH pairs.

### 6.2. Comparison to Results from the Literature

In the paper by Volonteri et al. (2022), dAGNs in the cosmological simulation Horizon–AGN are identified and related to the corresponding MBH binary mergers from the same simulation (Volonteri et al. 2022), and the numerical relation between the dAGNs and MBHB mergers is studied. The right column of their Figure 11 illustrates the CCFs of dAGNs with 5–10 kpc separations. According to their results, 30%–60% of these dAGNs observed at $z_{\rm dAGN} \sim 1$–3 coalesce before $z = 0$, the number increasing with decreasing $z_{\rm dAGN}$. This is due to the long evolution time of dAGNs with small mass ratios at high redshifts. These high-redshift dAGNs with small mass ratios are formed in the Horizon–AGN simulation because the criterion for MBH formation is based only on gas properties. More specifically, at high redshifts, when the gas reservoir is rich, some MBHs form in gas clouds that are too small to be identified as galaxies ("intergalactic" MBHs). These small "intergalactic" MBHs can be captured by galaxies later on and shine as dAGNs if some stochastic accretion occurs (Volonteri et al. 2022). Dual AGNs with one "intergalactic" MBH have small mass ratios and occur frequently at high redshifts (20%–30% of all dAGNs at $z = 2$–3). The evolution time of these systems is long and the resulting coalescence fractions are low, which leads to low coalescence fractions of dAGNs at high redshifts as shown in the right column of their Figure 11.

In comparison with Figure 5 of this paper, the CCFs in Volonteri et al. (2022) are in general lower at all $z_{\rm dAGN}$. This is because the initial dAGN separations considered in Volonteri et al. (2022, 30–50 kpc) are larger than that considered in this work (∼1 kpc), so the evolution time is longer and CCFs are lower in their case. As shown in Figure 5, in our calculation the CCFs increase with increasing $z_{\rm dAGN}$, contrary to the results of Volonteri et al. (2022). This is because we do not include those systems containing one "intergalactic" MBH in the analysis of this work (see Section 3 of Paper I). Overall, the results of Volonteri et al. (2022) indicate that dAGNs identified at small separations are generally indicators of effective mergers, which is in agreement with our results.

### 6.3. Impact of Simplifying Assumptions

The advantage of our semi-analytic model is its ability to provide calculations over a wide range of galaxy and MBH orbital properties at the cost of making some simplifying assumptions. The potential impact of our assumptions on the dynamical evolution of MBH pairs is discussed in Paper I. In this section, we consider the possible effects of these assumptions on the dAGN properties and their connection to MBH mergers.

We assume that the pMBH is fixed at the center of the host galaxy. If the motion of the pMBH and its corresponding Bondi–Hoyle–Lyttleton accretion rate are accounted for in the calculations, the resulting bolometric luminosity could potentially be lower (Hoyle & Lyttleton 1939; Bondi & Hoyle 1944; Bondi 1952) and the evolution time shorter due to the additional DF exerted on the moving pMBH. If so, there would be fewer dAGNs with $L_{\rm bol} > 10^{43}$ erg s$^{-1}$ and more MBH mergers at higher redshift, resulting in a larger coalescence fraction of dAGNs. This effect would be strongest in MBH pairs of comparable mass and weaker in those with small $q$. It would be manifested as an increase in the number of high-redshift LISA detections, since MBH pairs at high redshifts tend to have larger mass ratios.

The orbit of the sMBH is assumed to always reside in the midplane of the model remnant galaxy. If an inclined orbit were to take the sMBH outside of the galactic gas disk, the evolution time would increase and $L_{\rm bol}$ would decrease. We also assume that the sMBHs do not grow in mass during their orbital evolution from kiloparsec scales toward coalescence. Had they been able to do so, the increase in the total mass of the binary would render the inspiral time shorter and their bolometric luminosity higher.

As mentioned in Section 5, we considered the effect of RF only during the DF phase. Some studies have shown that RF can also affect the orbital evolution of sMBHs in circumbinary disks if there is no gap formed. Especially when sMBHs accrete at high rates, the radiation leads to strong winds pushing against the gas disk, blowing the gas away from the binary, which stalls the binary hardening in the circumbinary disks (del Valle & Volonteri 2018; Williamson et al. 2022). In contrast, when there is a gap in the disk, RF does not affect the evolution time of sMBHs (del Valle & Volonteri 2018). Our

model assumes the gap-opening regime (Paper I), so taking into account RF in circumbinary disks should not significantly affect the dAGN coalescence fraction and the LISA detection fraction predicted in this work.

Triplets of MBHs are likely to form at high redshifts, when the merger rate of galaxies is high. MBHs in these triplets may undergo the Kozai–Lidov oscillations, which may increase the eccentricity of the central MBHs (Kozai 1962) and increase the dAGN coalescence rate. Besides the Kozai–Lidov oscillations, the chaotic three-body interactions can also boost the coalescence rate (Blaes et al. 2002; Hoffman & Loeb 2007; Amaro-Seoane et al. 2010; Kulkarni & Loeb 2012; Bonetti et al. 2016; Ryu et al. 2018). These effects will be important if DF, which dominates the overall evolution of inspiralling MBHs (Paper I), brings multiple MBHs to the inner 1 pc at the same time.

We do not take into account gas consumption and star formation in the merger remnant galaxies. This means that during the orbital evolution from $\sim$1 kpc to coalescence, the gas fraction of a host remains at the same value inherited from the TNG50-3 data file. This assumption potentially increases the number of dAGNs with $L_{\rm bol} > 10^{43}$ erg s$^{-1}$, since in reality at least a fraction of the gas reservoir turns into stars. This reduces the gas fraction and increases the stellar density in the host galaxies. In the presence of RF, higher stellar densities result in more efficient orbital evolution of MBH pairs and more MBH mergers. Thus, in the presence of RF the coalescence fraction of dAGNs would be higher than determined here. In the absence of RF, the effect of this assumption cannot be easily predicted due to the complicated interplay of DF and the galactic parameters (Li et al. 2020b). The host galaxies with high gas fraction are most affected by this assumption.

## 7. Conclusions

dAGNs are a product of galaxy mergers and trace the population of future MBH coalescences. In this paper, we combined the calculations of MBH dynamical evolution from Paper I with estimates of AGN luminosity to explore how the luminosities and separations of dAGNs change as the MBH pair evolves in its host galaxy. In addition, we were able to calculate the fraction of the dAGN population at a redshift $z_{\rm dAGN}$ that lead to an MBH merger at redshift $z_{\rm coal}$, including determining the fraction that lead to a LISA S/N $> 8$.

We find that, in the absence of RF effects, the dAGN population in our model, with total bolometric luminosity $L_{\rm bol} > 10^{43}$ erg s$^{-1}$, peaks at $z_{\rm dAGN} \approx 0.4$ and is dominated by systems with separations $a \gtrsim 0.7$ kpc (Figure 1). However, a majority of these dAGNs will not lead to MBH mergers before $z = 0$ (Figure 3). In fact, the majority of low-$z_{\rm dAGN}$ dAGNs that are precursors to MBH mergers are separated by $\lesssim$0.5 kpc (Figure 2). This is a result of the orbital decay times of the sMBH—there is simply not enough time for most $a \sim 0.7$ kpc dAGNs at $z_{\rm dAGN} \approx 0.4$ to evolve to coalescence before $z = 0$. Therefore, a closer connection between dAGNs and MBH mergers can be most easily obtained by detecting dAGNs at $z_{\rm dAGN} \gtrsim 1$, where the coalescence fraction exceeds 0.5.

The orbital evolution of the sMBH depends on the properties of the post-merger galaxy and MBH pair (e.g., Paper I), so these conditions also impact the coalescence fractions of dAGNs. We find that dAGNs in post-merger galaxies with bulge masses $M_{\rm sb} \lesssim 10^{10}\ M_\odot$ and with MBH mass ratios of $q \approx 0.5$ have the highest coalescence fractions. Since these fractions increase with $z$, observational searches for dAGNs that lead to MBH mergers may consider prioritizing galaxies with less massive stellar bulges.

In Paper I we found the radiation feedback effects can significantly increase the evolution timescales for MBH pairs, particularly in galaxies with high gas fractions. This phenomenon ("negative DF") leads to a drop in the expected MBH coalescence rate and is seen in the dAGN properties when we include this effect (Figures 3 and 8). A signature of RF effects is a larger than expected number of dAGNs with wide separations, as this would indicate slow orbital decay predicted by negative DF.

The coalescence fractions shown in Figure 3 can be combined with the results of dAGN surveys to predict both the MBH merger rate and the rate of LISA signals with S/N $> 8$. We provide a recipe in Section 6.1 that can be followed to calculate these rates (either with or without RF effects) from observations of dAGNs. Comparison of these predicted rates to LISA measurements can be used to test our understanding of DF, including the importance of RF effects. The results like the ones presented here, in combination with the next generation of dAGN surveys, will thus be crucial in testing the physical models of MBH evolution at subkiloparsec scales.

## Acknowledgments

T.B. acknowledges the support by the National Aeronautics and Space Administration (NASA) under award No. 80NSSC19K0319 and by the National Science Foundation (NSF) under award No. 1908042.

## ORCID iDs

Kunyang Li https://orcid.org/0000-0002-0867-8946
Tamara Bogdanović https://orcid.org/0000-0002-7835-7814
David R. Ballantyne https://orcid.org/0000-0001-8128-6976
Matteo Bonetti https://orcid.org/0000-0001-7889-6810

## References

Amaro-Seoane, P., Audley, H., Babak, S., et al. 2017, arXiv:1702.00786
Amaro-Seoane, P., Sesana, A., Hoffman, L., et al. 2010, MNRAS, 402, 2308
Antonini, F., & Merritt, D. 2012, ApJ, 745, 83
Armitage, P. J., & Natarajan, P. 2005, ApJ, 634, 921
Ballo, L., Braito, V., Della Ceca, R., et al. 2004, ApJ, 600, 634
Barausse, E. 2012, MNRAS, 423, 2533
Begelman, M. C. 1985, ApJ, 297, 492
Begelman, M. C., Blandford, R. D., & Rees, M. J. 1980, Natur, 287, 307
Bianchi, S., Chiaberge, M., Piconcelli, E., Guainazzi, M., & Matt, G. 2008, MNRAS, 386, 105
Binney, J., & Tremaine, S. 2008, Galactic Dynamics: (2nd ed.; Princeton, NJ: Princeton Univ. Press)
Blaes, O., Lee, M. H., & Socrates, A. 2002, ApJ, 578, 775
Bondi, H. 1952, MNRAS, 112, 195
Bondi, H., & Hoyle, F. 1944, MNRAS, 104, 273
Bonetti, M., Haardt, F., Sesana, A., & Barausse, E. 2016, MNRAS, 461, 4419
Bonetti, M., Sesana, A., Haardt, F., Barausse, E., & Colpi, M. 2019, MNRAS, 486, 4044
Burke-Spolaor, S., Blecha, L., Bogdanovic, T., et al. 2018, arXiv:1808.04368
Chandrasekhar, S. 1943, ApJ, 97, 255
Comerford, J. M., Gerke, B. F., Stern, D., et al. 2012, ApJ, 753, 42
De Rosa, A., Vignali, C., Bogdanović, T., et al. 2019, NewAR, 86, 101525
del Valle, L., & Volonteri, M. 2018, MNRAS, 480, 439
Gardner, J. P., Mather, J. C., Clampin, M., et al. 2006, SSRv, 123, 485
Ge, J.-Q., Hu, C., Wang, J.-M., Bai, J.-M., & Zhang, S. 2012, ApJS, 201, 31

Gruzinov, A., Levin, Y., & Matzner, C. D. 2020, MNRAS, 492, 2755
Guainazzi, M., Piconcelli, E., Jiménez-Bailón, E., & Matt, G. 2005, A&A, 429, L9
Hoffman, L., & Loeb, A. 2007, MNRAS, 377, 957
Hoyle, F., & Lyttleton, R. A. 1939, PCPS, 35, 405
Inayoshi, K., Haiman, Z., & Ostriker, J. P. 2016, MNRAS, 459, 3738
Jiang, Y.-F., Stone, J. M., & Davis, S. W. 2019, ApJ, 880, 67
Kelley, L., Charisi, M., Burke-Spolaor, S., et al. 2019, BAAS, 51, 490
Kelley, L. Z., Blecha, L., & Hernquist, L. 2017, MNRAS, 464, 3131
Khan, F. M., Mirza, M. A., & Holley-Bockelmann, K. 2020, MNRAS, 492, 256
Kim, D. C., Yoon, I., Evans, A. S., et al. 2020, ApJ, 904, 23
Kim, H., & Kim, W.-T. 2007, ApJ, 665, 432
Komossa, S., Burwitz, V., Hasinger, G., et al. 2003, ApJL, 582, L15
Koss, M., Mushotzky, R., Veilleux, S., & Winter, L. 2010, ApJL, 716, L125
Kozai, Y. 1962, AJ, 67, 591
Kulkarni, G., & Loeb, A. 2012, MNRAS, 422, 1306
Li, K., Ballantyne, D. R., & Bogdanović, T. 2021, ApJ, 916, 110
Li, K., Bogdanović, T., & Ballantyne, D. R. 2020a, ApJ, 905, 123
Li, K., Bogdanović, T., & Ballantyne, D. R. 2020b, ApJ, 896, 113
Li, K., Bogdanović, T., Ballantyne, D. R., & Bonetti, M. 2022, ApJ, 933, 104
Liu, X., Shen, Y., Strauss, M. A., & Hao, L. 2011, ApJ, 737, 101
Lusso, E., Comastri, A., Simmons, B. D., et al. 2012, MNRAS, 425, 623
Milosavljević, M., & Phinney, E. S. 2005, ApJL, 622, L93
Murphy, E. J. 2018, in IAU Symp. 336, Astrophysical Masers: Unlocking the Mysteries of the Universe, ed. A. Tarchi, M. J. Reid, & P. Castangia (Cambridge: Cambridge Univ. Press), 426
Nandra, K., Barret, D., Barcons, X., et al. 2013, arXiv:1306.2307
Nelson, D., Pillepich, A., Springel, V., et al. 2019b, MNRAS, 490, 3234
Nelson, D., Springel, V., Pillepich, A., et al. 2019a, ComAC, 6, 2
Ostriker, E. C. 1999, ApJ, 513, 252
Ostriker, J. P., McCray, R., Weaver, R., & Yahil, A. 1976, ApJL, 208, L61
Park, K., & Bogdanović, T. 2017, ApJ, 838, 103
Park, K., & Ricotti, M. 2011, ApJ, 739, 2
Park, K., & Ricotti, M. 2012, ApJ, 747, 9
Park, K., & Ricotti, M. 2013, ApJ, 767, 163
Piconcelli, E., Vignali, C., Bianchi, S., et al. 2010, ApJL, 722, L147
Pillepich, A., Nelson, D., Springel, V., et al. 2019, MNRAS, 490, 3196
Quinlan, G. D. 1996, NewA, 1, 35
Quinlan, G. D., & Hernquist, L. 1997, NewA, 2, 533
Ricci, C., Bauer, F. E., Treister, E., et al. 2017, MNRAS, 468, 1273
Ricotti, M., Ostriker, J. P., & Mack, K. J. 2008, ApJ, 680, 829
Ryu, T., Perna, R., Haiman, Z., Ostriker, J. P., & Stone, N. C. 2018, MNRAS, 473, 3410
Smith, K. L., Shields, G. A., Bonning, E. W., et al. 2010, ApJ, 716, 866
Thorne, K. S., & Braginskii, V. B. 1976, ApJL, 204, L1
Toomre, A. 1964, ApJ, 139, 1217
Toyouchi, D., Hosokawa, T., Sugimura, K., & Kuiper, R. 2020, MNRAS, 496, 1909
Valiante, R., Schneider, R., Volonteri, M., & Omukai, K. 2016, MNRAS, 457, 3356
Volonteri, M., Haardt, F., & Madau, P. 2003, ApJ, 582, 559
Volonteri, M., Pfister, H., Beckmann, R., et al. 2022, MNRAS, 514, 640
Wang, J.-M., Chen, Y.-M., Hu, C., et al. 2009, ApJL, 705, L76
Williamson, D. J., Bösch, L. H., & Hönig, S. F. 2022, MNRAS, 510, 5963
Yu, Q. 2002, MNRAS, 331, 935